FINGER-LIKE SMOLDERING OVER THIN CELLULOSIC SHEETS IN MICROGRAVITY

S. L. OLSON,[1] H. R. BAUM[2] AND T. KASHIWAGI[2]

[1]*Microgravity Combustion Science Branch*
NASA Lewis Research Center
Cleveland, OH 44135, USA
[2]*Building and Fire Research Laboratory*
National Institute of Standards and Technology
Gaithersburg, MD 20899, USA

Microgravity smolder spread over a thin cellulosic fuel was studied with the Radiative Ignition and Transition to Spread Investigation (RITSI) apparatus in the Glovebox Facility on the STS-75 USMP-3 space shuttle mission. Radiative smoldering ignition was initiated by a focused beam from a tungsten/halogen lamp at the center of the smolder-promoted filter paper. The external airflow velocity was varied from 0.5 cm/s to 6.5 cm/s. The ignition and subsequent smolder spread events were recorded by a video camera, a 35-mm camera, and six thermocouples (two in the gas phase and four in the sample). Nonpiloted smoldering ignition of the paper in microgravity by external thermal radiation was demonstrated for the first time. Unlike the uniform normal gravity smolder front, a complex, unexpected finger-shaped char growth pattern was observed in microgravity. The preferred direction of smolder finger propagation was upstream into the fresh oxidizer. Downstream smolder was less viable and slower. Increasing external flow velocity increased the number of localized smoldering fronts, the number of the char fingers they left behind, and the frequency of bifurcations from the fingers. An analytical "oxygen shadow" model indicated that each localized smolder front cast an oxygen shadow that depleted the ambient oxygen in an egg-shaped region around itself. These oxygen shadows are a plausible explanation of the fingering smolder patterns observed in the experiments.

Introduction

Smoldering is a common mode of initiation of fires in normal gravity and creates hazardous conditions due to high CO yield. Few smolder studies have been published even for normal gravity. Although smoldering heat release rates are smaller than those from flaming, the smolder surface temperatures are as high as 1000 K, and induced buoyant flow cannot be neglected in normal gravity. The induced buoyant flow makes it difficult to quantify or control the supply rate of oxygen to the smoldering front in normal gravity. Because oxygen supply to the smoldering front is a critical parameter that controls smolder spread, this makes it difficult to predict smoldering behavior in the subbuoyant flow typical of spacecraft in microgravity.

Moussa et al. [1] found for thin cellulose cylinders that the critical smolder spread mechanism is char oxidation, which provides the heat flux needed to sustain pyrolysis. Extinction was observed when the feedback portion of the heat flux (heat release minus heat losses) was insufficient to sustain pyrolysis.

Ohlemiller [2] found that forward smolder rates over wood (downstream smolder) increased with air supply, due to the acceleration of oxygen transfer rates to the wood surface and the subsequent highly exothermic char oxidation rate. Reverse smolder (upstream smolder) was slower due to convective cooling. It was also insensitive to the airflow, possibly due to the comparable magnitudes of the buoyant flow (estimated here to be 20 cm/s) and the experimentally imposed flow (10 to 25 cm/s).

Two previous smolder experiments have been conducted in space [3,4], using thick, porous polyurethane foam. In a quiescent environment, even at elevated oxygen concentrations, smolder through the foam was not self-sustaining. With even a weak flow (1–2 mm/s), smolder in air was self-sustaining, and uniform smolder spread rates were between upward and downward normal gravity smolder rates, in keeping with oxygen supply to the smolder front.

Fingering combustion was observed for thin solids on Earth [5] when the buoyant oxidizer flow is very strictly limited by using a Hele–Shaw-type thin horizontal channel with very slow forced flow, and with significant heat losses to the solid substrate. A stability analysis of filtration combustion in porous media [6] finds for these types of conditions there is a cellular (fingering) solution to the Saffman–Taylor formulation of the problem, where mass diffusion is
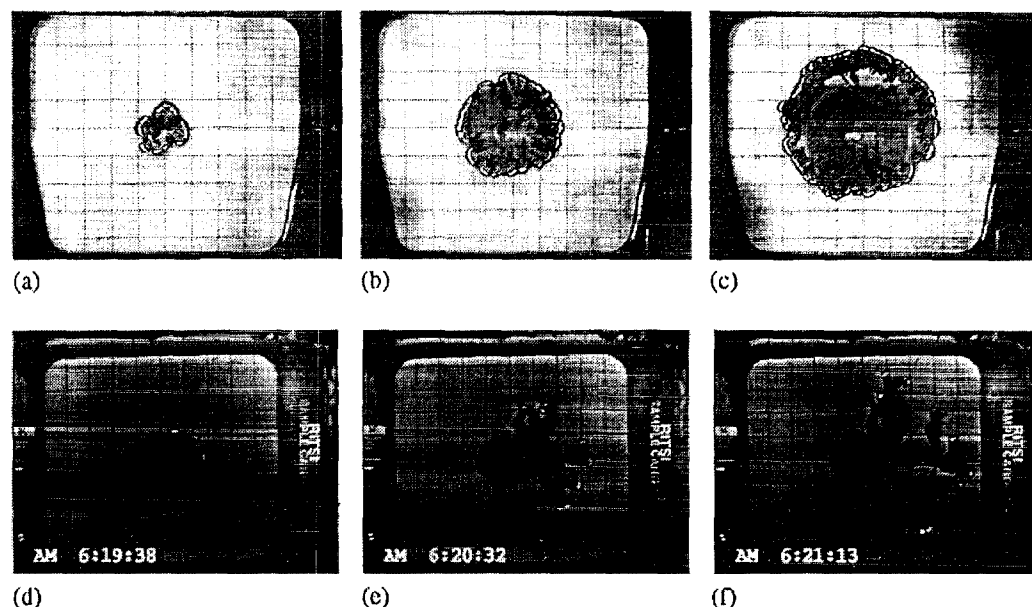
FIG. 1. Time sequence showing the development of smoldering patterns in normal gravity (a–c) and at 0.5 cm/s imposed flow in microgravity (d–f). Black grid on the sample surface is 1 cm × 1 cm. Normal gravity horizontal smolder in a natural convection environment is symmetric from shortly after ignition. In contrast, microgravity smolder exhibits non-uniform fingering that shows a strong preference toward the upstream direction (flow enters from the right of each picture).

strongly destabilizing even though hydrodynamics is weakly stabilizing.

Flight Hardware

Smolder experiments were performed in the space shuttle during the STS-75 USMP-3 mission, inside a Glovebox Facility [7]. The test section of the experiment module was 85 mm wide × 95 mm high × 171 mm long. A transparent lid provided optical viewing and access for changeout of sample cards. Fan-drawn flow passed smoothly through the test section at speeds from 0 to 6.5 cm/s. Fan voltage was calibrated with a low-velocity hot wire anemometer. Smoke flow visualization confirmed the uniformity of the flow through the test section.

Samples were 10-cm by 8.7-cm sheets of Whatman ashless filter 44 (0.017 cm thickness),* doped with smolder-promoting potassium acetate in uniform concentrations (±5%) sufficient to ensure that smoldering ignition is independent of ion concentration [8]. Chromel-alumel thermocouples (0.05

———————

*Certain company products are mentioned in the text to specify adequately the experimental procedure and equipment used. In no cases does such identification imply recommendation or endorsement by the National Aeronautics and Space Administration or the National Institute of Standards and Technology, nor does it imply that the products are necessarily the best available for the purpose.

mm) were preinstalled on each sample; four sewn into the surface, and two 2 mm above the surface in the gas phase. Data were recorded throughout the test at 10 Hz, with an estimated error of ±10 K. Color video pictures were taken of the sample surface. A near-infrared tungsten/halogen radiant heater recessed in the duct wall was used to ignite the samples. The flux distribution of the 15.5-W, 10-s ignition beam was Gaussian, with a radius of approximately 1 cm at the sample surface.

Smolder Appearance

Smolder patterns developing under two different gravity environments are shown in Fig. 1. In normal gravity, as shown in Fig. 1a–c, the glowing smolder front remained symmetric although segmented (probably due to local char curling and breakage). The smolder area pattern was nearly uniform and continuous. In microgravity, however, a very complex finger-shaped char pattern was observed from the outset of the experiment. Discrete glowing smoldering fronts were localized at the fingertips as seen in Fig. 1d–f. The direction of growth of the char fingers was almost solely upstream during this weakest of the microgravity tests. Any smolder fronts that turned downstream quenched within approximately 0.5 cm, or turned back upstream. This is believed to be due to lack of oxygen with dilution from degradation products and/or consumption of oxygen from
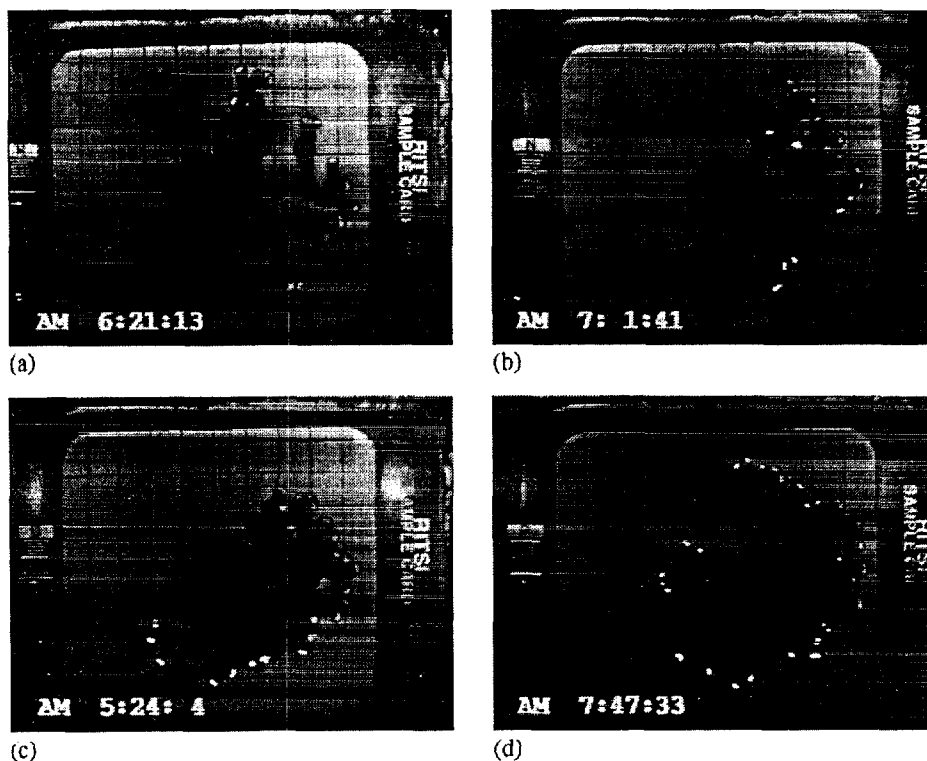
FIG. 2. Microgravity smolder patterns with red diodes illuminating the sample surface. Flow is from the right in all cases. (a) microgravity sparse fingerlike upstream smoldering in the limit of 0.5 cm/s air flow; (b) microgravity upstream smolder fingers in a 2 cm/s airflow; (c) increased density smolder fingers in 5 cm/s airflow. (d) dense microgravity smolder fingers in a 6.5 cm/s airflow.
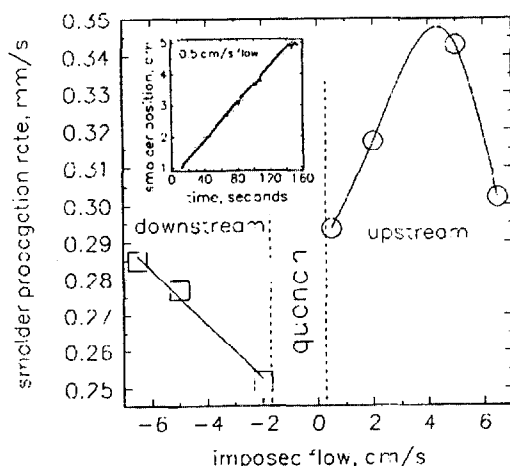

FIG. 3. Smolder spread rates as a function of imposed flow; positive flow is upstream spread into fresh oxidizer, negative flow is downstream spread with the flow. Inset shows a position versus time trace for the 0.5 cm/s upstream spread with the slope being the spread rate. The spread rate data points are sized to reflect the typical 95% confidence interval on the slope of the smolder front position versus time data.

the upstream smolder fronts (oxygen shadow effect), as discussed later.

Figure 2 shows the smolder patterns obtained at four imposed-flow velocities in microgravity. As the velocity increased, the number of smolder fronts (fingers) increased. The size of the smolder spots was independent of velocity. After the upstream smolder reached the edge of the sample (not shown), smolder fronts turned downstream. Eventually, most of the sample was consumed, with the exception of the 0.5 cm/s smolder test, where downstream smolder was not viable. Although these fingerlike smolder patterns seem chaotic, there is a great deal of order in the system.

Smolder Spread Rates

Direct upstream and downstream spread rates were measured by tracking a smolder front propagating in those directions. Downstream smolder rates were measured only after the upstream smolder was complete, to avoid influence on the oxygen flow to the downstream fronts. The upstream and downstream smolder spread rates are shown in Fig. 3 as a function of imposed velocity. Upstream smolder spread increases with increasing velocity from 0.5 to 5 cm/s, but above 5 cm/s, spread rate appears
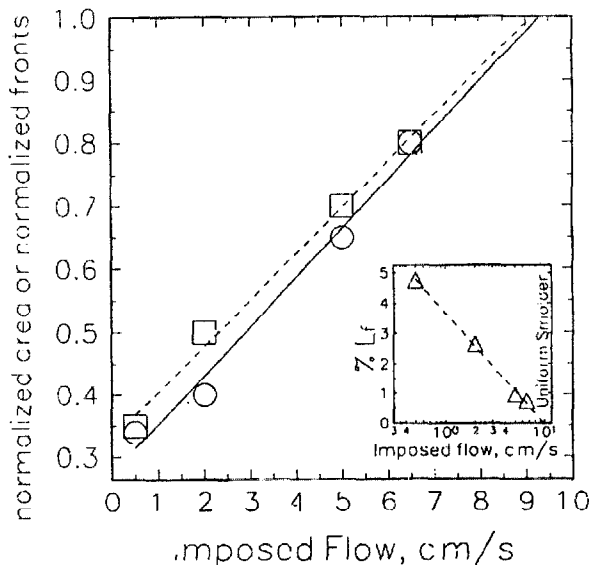
FIG. 4. Normalized area smoldered and the number of smolder fronts per normalizing area linearly increase with imposed flow. The ratio of normalized area to normalized number of fronts, which is smoldered area per front, is unity throughout the flow domain. This indicates that each smolder front is of fairly constant size. The inset shows the normalized distance between smolder fronts linearly decreases with the log of the imposed flow. The imposed velocity at which a single uniform front should occur (unity normalized area, with one front per normal area and zero normalized distance between fronts) is extrapolated to be about 9 to 10 cm/s imposed flow in each case. O, normalized area smoldered; □, normalized number of fronts; △ normalized spacing between fronts.

to decrease with increasing velocity. Although more data are needed to verify this trend, the data are similar to trends observed in opposed-flow flame spread, where a maximum in flame spread is noted at low-speed airflows in microgravity [9]. The quench limit for upstream smolder is between 0.0 and 0.5 cm/s flow.

Downstream smolder spread (measured after the upstream smolder was completed) increases with imposed flow over the range studied. It is slower and less viable than the upstream flame spread—the fastest downstream smolder is slower than the weakest upstream smolder. However, in normal gravity, due to higher induced-flow velocities, the reverse is true—downstream smolder is faster than upstream smolder [2]. To merge the two trends, at some higher flow velocity in microgravity, the downstream smolder must become faster than the upstream smolder. The downstream smolder quench limit was between −0.5 and −2 cm/s, as demonstrated by the extinction of all smolder fronts that turned downstream in the −0.5 cm/s imposed flow test. The nonflammable region between the upstream and downstream quench limits is simply labeled "quench" in

Fig. 3. These trends are remarkably consistent with those in Refs. [9] and [10] for flame spread.

Smolder Efficiency

Most of the smolder fronts did not propagate directly upstream or downstream but at angles to the flow. To get a better understanding of the overall smolder process, the smoldered area was measured as a function of time and normalized by the semicircular area $\pi r(t)^2/2$, where $r(t)$ is the directly upstream smolder position as a function of time. Using a semicircular area is appropriate because at higher flowrates (in normal gravity), the upstream front is semicircular. The normalized area in each test approached a constant value, which varied with flow velocity as shown in Fig. 4. The fractional coverage increases with increasing velocity, approaching unity at 9 to 10 cm/s. Normal gravity buoyant flows are higher than this, so at high enough velocities, a uniform smolder front is observed as in Fig. 1a–c. Similarly, the number of smolder fronts per semicircular area in Fig. 4 shows a linear increase with imposed flow.

The inset of Fig. 4 shows the increased population density expressed as the normalized front spacing. The normalized average front spacing L_f, which is the fraction of the total semicircular circumference between each front, was estimated

$$L_f(t) = \frac{[\pi r(t) - 0.3F(t)]}{\pi r(t)F(t)} \qquad (1)$$

where the total circumference of the smolder upstream semicircle was $\pi r(t)$, the average width of each smolder front was 0.3 cm, and $F(t)$ was the number of smolder fronts as a function of time. The normalized distance between smolder fronts, $L_f(t)$, approaches a steady value by the end of the upstream spread, and this steady value was found to increase logarithmically with velocity. The velocity at which a single uniform front should occur (zero normalized distance between fronts) is extrapolated to be about 9 to 10 cm/s imposed flow, in good agreement with the preceding normalized smoldered area and normalized smolder front measurements.

Population Studies

The smolder front population events were tracked in time. Bifurcation of the fingers, where one smolder front split into two, was observed. Extinction of smolder fronts was also observed. The collision of two smolder fronts, merging, is where two fronts become one. To characterize the dynamics of this smolder front population, each event was tracked in time, as shown in Fig. 5. These events were tracked until the smolder fronts reached the upstream edge of the
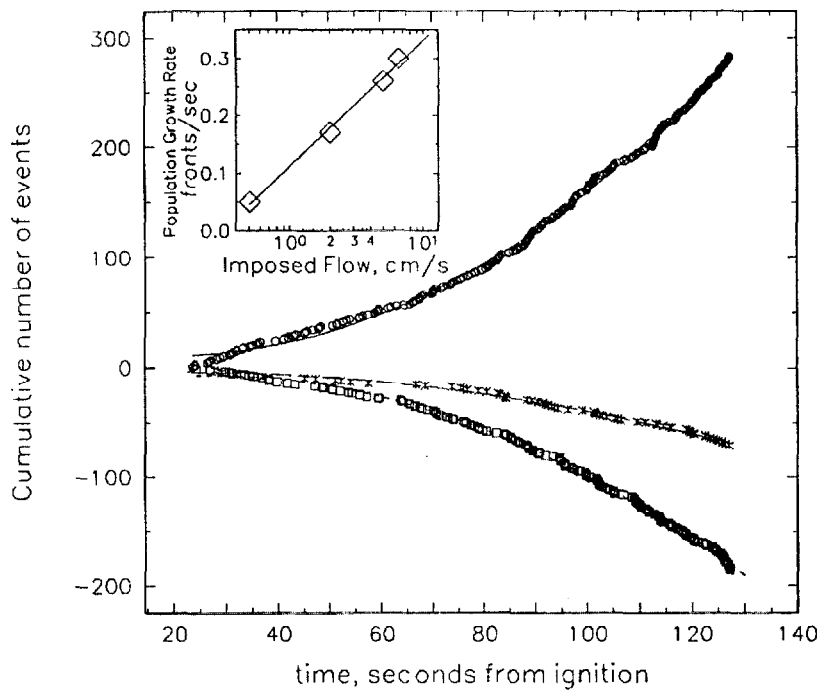
FIG. 5. Dynamics of the population of smolder fronts as a function of time: bifurcations add one to the population; extinctions and merges decrease the population by one. The inset shows the overall population growth rate increases with imposed flow. O, bifurcations; □, extinctions; ✗, merges; ◇, population growth rate.
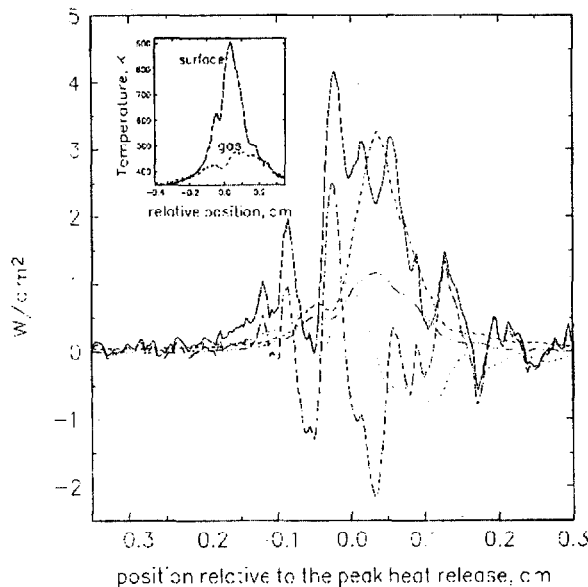

FIG. 6. Energy balance terms from equation 2 using gas and surface thermocouple data (inset) from the test with 2 cm/s flow velocity. All terms but the net heat release are calculated from the measured temperatures. Net heat release is derived to balance equation 2. The greater peak had a heat release of near 4 W/cm², whereas the lesser peak had a heat release of approximately 2 W/cm². These two peaks were observed in both upstream and downstream smolder propagation, as well as in smolder at angles to the flow direction. Forward solid-phase conduction is the primary mechanism of heat transfer for the smolder propagation. Surface radiative loss from the glowing char is the primary heat loss term. ——— net heat release; ····· solid energy content; ————— solid conduction; –·–·–·– gas conduction loss; ------ surface radiative loss.

sample, where edge effects began to play a role. The independently tracked total population was compared with the sum of distinct events to confirm that no events were missed. The cumulative number of each event increased quadratically with time, as shown by the curves drawn through the data points for each event. The *rates* of each event increased linearly with time, in proportion with the semicircular surface length available for smolder.

Solid-Phase Energy Balance

Measured thermocouple data obtained during smolder front passage are used to evaluate each term of a transient, finite-thickness, two-dimensional, solid-phase energy balance, given in equation 2 and plotted in Fig. 6. This reveals more detail about the structure of the smolder front.

$$Q''_{net} = \rho_s \tau_s C_s \frac{\partial T_s}{\partial t} + k_s \tau_s \frac{\partial^2 T_s}{\partial x^2}$$
$$+ k_g \frac{\partial T_g}{\partial y} + \varepsilon\sigma[T_s^4 - T_\infty^4] \quad (2)$$

where the half-thickness area density $\rho_s \tau_s$ = 0.00385 g/cm²; solid heat capacity C_s = 1.26J/g K, T_s = surface temperature; T_∞ = ambient temperature; emissivity ε = 0.85, σ = 5.729 × 10⁻¹² W/cm² K⁴, k_g = 5.236 × 10⁻⁴W/cm K (air@700 K), and k_s = 4.006 × 10⁻⁴W/cm K (surface).

The surface and gas-phase temperature data are shown in the inset to Fig. 6. The surface temperature at the onset of exothermic pyrolysis reactions was 600 K, with a peak temperature of over 900 K,
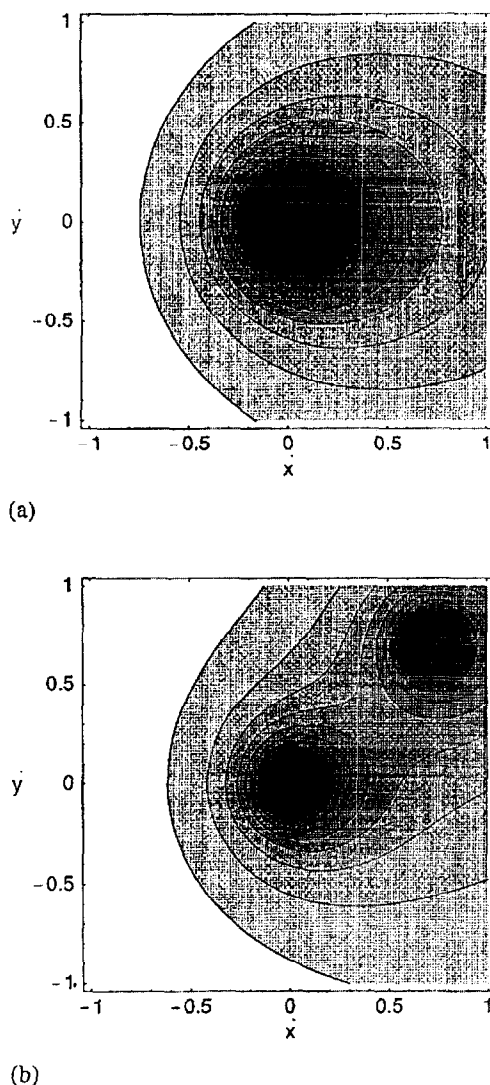
(a)

(b)

FIG. 7. (a) Egg-shaped oxygen shadow region around a single smolder spot computed from the oxygen transport model. Surface mass fraction contours (grey) induced by a smolder spot (shown in black for $Y/Y_\infty = 0$) are plotted in increments of Y/Y_∞ of 0.1. White is ambient oxygen levels. X and Y are in units of the Stokes length scale $2D/U_\infty$. (b) Surface mass fraction contours induced by two spots located one Stokes length apart, with the line connecting them aligned at 45° angle with the flow direction. The oxygen shadow in the region between the two spots is much deeper than it is around a single spot. It is not hard to visualize geometries where an array of spots can drive the local flux between spots to such low levels that smoldering can no longer be sustained in over a substantial fraction of the surface.

corresponding to the glowing tips of the smolder fingers. Two distinct temperature and heat release peaks were observed a few millimeters apart during smolder propagation. The lesser peak may be an oxidative pyrolysis reaction (paper blackening), which occurs from 470–700 K, measured with a differential

scanning calorimeter for the same material in air; and the greater peak may be a char oxidation peak (glowing char), which occurs from 770–1030 K. The dip in temperature between the two peaks was unexpected but very consistent in all tests. It is discussed further in the following.

Oxygen Transport Model

Because combustion occurs at the surface of the thin paper samples, the smolder is like a pathological kind of diffusion flame. To describe the oxygen transport to the smolder spots as it relates to the fingering patterns observed in the experiments, a mathematical model of oxygen consumption by discrete smolder elements on a thermally thin surface was formulated. The convective-diffusive balance in the gas phase with an Oseen approximation for low Reynolds number conditions is solved over a surface with discrete smolder spots. Away from smolder spots, the surface oxygen gradient is zero, but the small smolder sites of radius l are assumed to be "catalytic" and consume oxygen at a rate sufficient to drive the surface oxygen concentration to zero across each smolder spot. Far from the surface, oxygen concentrations are ambient.

The solution for the local oxygen concentration and the total flux to each smolder spot are obtained using a matched asymptotic expansion for $\lambda = U_\infty l/2D \ll 1$ to leading order in λ. (The natural length scale is the gas-phase Stokes length scale, $l_g = 2D/U_\infty$, where D is the mass diffusivity of oxygen in air.) Then, the local oxygen concentration Y is

$$Y = Y_\infty - \frac{M}{4\pi\rho Dl} \phi(r, z, l)$$

$$\cdot \exp\left[\frac{U_\infty}{2D}\left(x - x_0 - \sqrt{r^2 + z^2}\right)\right] \quad (3)$$

where

$$\phi(r, z, l) = \arctan$$

$$\cdot \left[\frac{2l^2}{r^2 + z^2 - l^2 + \sqrt{(r^2 + z^2 - l^2)^2 + 4l^2z^2}}\right] \quad (4)$$

and $r = [(x - x_0)^2 + (y - y_0)^2]^{1/2}$ is the magnitude of the surface vector from source to field point. $M = 8\rho DlY_\infty$ is the total mass flux to both sides of the spot. The exponential term in equation 3 shows that the oxygen shadow is a strong function of imposed flow and is strongly biased to the downwind side of each spot. Each smolder spot produces an egg-shaped oxygen shadow wake, as shown in Fig. 7a for a single spot.

The radial dependence of the surface oxygen mass flux is $m_0(r) = M/[4\pi/(l^2 - r^2)^{1/2}]$. This implies that the burning rate on each smolder spot is peaked in
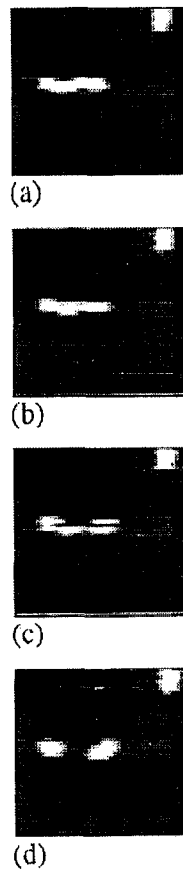
(a)

(b)

(c)

(d)

FIG. 8. Sequence of close-up images from a bifurcating front in 6.5 cm/s flow velocity (from the right). Images are 1/3 second apart. Image size is 1 cm × 1 cm. Single front, 4 mm wide (a) shows separation into three distinct zones (b, c), and then the middle zone extinguishes (d) to complete the bifurcation. The model indicates that the extinguishment of the central region of the smolder front is due to the reduced oxygen mass flux to that region caused by the peripheral smolder elements.

a finite-thickness ring near the edges of the smolder spot. This is consistent with two observed heat release peaks in the thermocouple data, which correspond to the front and the rear of the smolder ring passing the measurement point.

For an array of spots, the determination of the total flux to each spot, M_k, couples the solution for each spot as

$$Y_\infty = \frac{M_k}{4\pi\rho Dl} \frac{\pi}{2} + \sum_{i=1,i\neq k}^{N} \frac{M_i}{4\pi\rho Dl}$$
$$\cdot \arctan\left(\frac{\lambda}{\sqrt{R_{ik}^2 - \lambda^2}} \exp(X_k - X_i - R_{ik})\right) \quad (5)$$

where X_k, X_i, are the coordinates of each smolder spot, and R_{ik} is the distance between elements, all measured in units of Stokes length l_g. This shows that the dimensionless oxygen mass flux to each smolder spot, $M_k/4\pi\rho DlY_\infty$, depends strongly on the

proximity of all other spots, weakly upon λ, the non-dimensional smolder spot radius, and nothing else.

Fig. 7b shows a case where two spots are located one Stokes length, l_g, apart. The upstream spot flux, M_i, is slightly reduced (99%) from the value of a single spot in Fig. 7a. The downstream spot flux is reduced more (97%) due to the wake of the upstream spot's oxygen shadow. In the region between the two spots, the absolute O_2 mass fraction is below 0.14, and it drops below 0.1 over a small area. It is most unlikely that smoldering could be sustained at such low levels.

Discussion of Results

The complex fingerlike smoldering in microgravity was unexpected. Fingering smolder is not observed in this experiment in normal gravity, so nonuniformities in the ion concentration or in the sample uniformity (porosity, density, thickness) are not the cause. A reasonable explanation is that the very low local oxygen flux limits the size of the smolder spot and suppresses smoldering adjacent to the spot due to local depletion of the ambient oxygen concentration. Smoldering produces a roughly 20 cm/s buoyancy-induced airflow in normal gravity, so the oxygen flux is sufficient to support a uniform smolder front. In microgravity, an airflow velocity up to 6.5 cm/s is not sufficient, although extrapolation of the data indicates that a uniform front would be obtained for an airflow velocity of 9 to 10 cm/s.

A physical manifestation of this local extinction process is the smolder bifurcation process. Bifurcations tended to occur when the width of the smolder front grew too wide. Bifurcation occurred when the smolder front width exceeded approximately 0.3 cm. This is of the same order as the diffusive gas-phase Stokes length scale ($l_g = 2D/U_\infty$) and is significantly larger than the solid-phase length scale $l_s = \alpha_s/V_s$, where α_s is the solid thermal diffusivity and V_s is the velocity of the smolder spot. Fig. 8 shows a close-up of the bifurcation process where the central region of the smolder front extinguishes. The bifurcation process occurs in approximately one second, regardless of imposed flow. This timescale is consistent with solid-phase timescales $t_s = l_s/V_s \approx 2/3$ s, because the primary heat release and heat losses are from the solid phase. In contrast, gas-phase timescales vary with flow $t_g = l_g/U_\infty \approx 0.8$ s to less than 0.1 s at the highest flows. This bifurcation-extinction process is consistent with the oxygen transport model, but a full theory of smoldering detailed structure (with inclusion of thermal oxidative degradation, solid-phase energy, and mass balances) is needed to predict the time evolution of the patterns.

Conclusions

Although uniform smolder fronts occur in normal gravity natural convection environments, a complex,

finger-shaped char pattern was observed in micro-gravity. Each "fingertip" had a glowing smolder front that propagated, frequently bifurcated, and occasionally extinguished. Smolder fronts preferentially propagated upstream into fresh oxidizer. Downstream propagation was slower and less viable. At low imposed flows, onset of downstream smolder was delayed until completion of upstream smolder, due to the oxygen shadow cast by the upstream smolder fronts.

Normalized smolder area, a fraction of the area available that smoldered, linearly increased with flow and approached unity (uniform front) at imposed-flow velocities of 9 to 10 cm/s. Smolder front spacing decreased with imposed flow and approached zero (uniform front) at the same 9 to 10 cm/s flow. Average smolder front width ("fingertip") was independent of flow velocity. The smolder fronts exhibited bifurcation, merging, and extinction rates that were directly proportional to the semicircular circumference available for smolder.

Analysis of oxygen transport revealed that each smolder front cast an oxygen shadow that influenced the oxygen mass flux to adjacent smolder fronts. The oxygen mass flux to each smolder front depended strongly on the proximity of other smolder fronts, and weakly on the nondimensional smolder spot size. The derived ring-shaped maximum in the oxygen mass flux implied that the smolder front is ring-shaped, which is consistent with the observed two heat release peaks.

Acknowledgments

REFERENCES

1. Moussa, N. A., Toong, T. Y., and Garris, C. A., in *Sixteenth Symposium (International) on Combustion*, The Combustion Institute, Pittsburgh, 1977, pp. 1447–1457.
2. Ohlemiller, T. J., in *Third International Symposium on Fire Safety Science*, Elsevier Science, New York, 1991, pp. 565–574.
3. Stocker, D. P., Olson, S. L., Urban, D., Torero, J. L., Walther, J. L., and Fernandez-Pello, A. C., in *Twenty-Sixth Symposium (International) on Combustion*, The Combustion Institute, Pittsburgh, 1996, pp. 1361–1368.
4. Walther, D. C., Fernandez-Pello, A. C., and Urban, D. L., in *Fourth International Microgravity Combustion Workshop*, NASA Conference Publication 10194, 1997, pp. 369–374.
5. Zik, O. and Moses, E., in *Twenty-Seventh Symposium (International) on Combustion*, The Combustion Institute, Pittsburgh, 1998, pp. 2815–2820.
6. Aldushin, A. P. and Matkowsky, B. J., *Combust. Sci. Technol.* 133:293–341 (1998).
7. Instrument Interface Agreement for Middeck Glovebox Facility and Investigations, JA-1993, NASA MSFC CCBD 213-9500008, January 31, 1995.
8. Ihrig, A. M. and Smith, S. L., *J. Fire Sci.* 12:357–375 (1994).
9. Olson, S. L., *Combust. Sci. Technol.* 76:233–249 (1991).
10. McGrattan, K. B., Kashiwagi, T., Baum, H. R., and Olson, S. L., *Combust. Flame* 106:377–391 (1996).

COMMENTS

Paul Ronney, University of Southern California, USA.
My congratulations on a fascinating set of experiments. Your explanation of the fingering instability discusses oxygen transport but does not address the issue of why heat diffusivity does not smooth out the fingers. I propose a different explanation for your fingering instabilities. Oxygen transport can occur only through the gas phase on a length scale D_{O_2}/U, where D_{O_2} is the oxygen diffusivity and U is the opposed flow velocity. Heat transport can occur in the gas phase on a length scale α/U, where α is the thermal diffusivity, or α_s/U_s, where U_s is the smolder velocity. At large U, gas-phase heat transport dominates and the effective Lewis number is α/D_{O_2}, which is close to unity for gases. In contrast, at low U, radiative loss may suppress gas-phase heat transport but cannot affect oxygen transport, thus the effective Lewis number is closer to α_s/D_{O_2}, which is much smaller than unity. Thus a diffusive-thermal mechanism based on a hybrid gas-phase/solid-phase Lewis number may describe your observations. This explanation would also explain the observations of the paper by Zik and Moses [1], where, in their case, conductive loss to the channel ceiling when the height is sufficiently small would suppress gas-phase heat transport.

REFERENCE

1. Zik, O. and Moses, E., in *Twenty-Seventh Symposium (International) on Combustion*, The Combustion Institute, Pittsburgh, 1998, pp. 2815–2820.

Author's Reply. We thank Paul for his kind remarks.

However, we do not think that fingering is a Lewis Number effect in the sense he describes. The controlling/limiting transport mechanism for the fingering behavior is mass transport, via gas-phase convection/diffusion. Gas-phase heat diffusivity has a very small effect; the predominant mode of heat transfer for propagation is solid-phase conduction. The appropriate gas-phase diffusive length scale is $D_{O_2-N_2}/U$, which varies from 0.2 mm at 10 cm/s imposed flow to 4 mm at 0.5 cm/s imposed flow. The appropriate solid-phase conduction length scale is $\alpha_s/V_s \approx 0.2$ mm (constant).

If we ratio these length scales, we see they are of order unity at imposed flows of 10 cm/s, where we predict a uniform smolder front would occur. As flow is reduced, the diffusive length scale becomes much larger than the thermal length scale, and we observe increasingly sparse fingering. The imbalance in length scales is entirely consistent with our hypothesis that fingering is due to the local depletion of ambient oxygen around the smolder fronts, which suppresses smoldering adjacent to the fronts. Indeed, the model presented in our paper assumes that the fuel is burning as fast as the available oxygen supply permits. However, the supply is so feeble that the isolated spots are the only possible arrangement consistent with any combustion at all.

Other papers are consistent with this view. Altenkirch et al. (this session) describe an every increasing mismatch in the (constant) thermal and (ever-growing) mass diffusion length scales throughout their space experiment, leading to the flame's eventual extinction due to insufficient oxygen diffusion. Zik and Moses also conclude that fingering is due to the local oxygen deficiency at their very low forced flow rates.